Seasonal seismic activity on Mars

M. Knapmeyer, S.C. Stähler, I. Daubar, F. Forget, A. Spiga, T. Pierron, M. van Driel, D. Banfield, E. Hauber, M. Grott, et al.

▶ **To cite this version:**

M. Knapmeyer, S.C. Stähler, I. Daubar, F. Forget, A. Spiga, et al.. Seasonal seismic activity on Mars. Earth and Planetary Science Letters, 2021, 576, pp.117171. 10.1016/j.epsl.2021.117171 . hal-03362753

HAL Id: hal-03362753
https://hal.science/hal-03362753

Submitted on 2 Oct 2021

HAL is a multi-disciplinary open access archive for the deposit and dissemination of scientific research documents, whether they are published or not. The documents may come from teaching and research institutions in France or abroad, or from public or private research centers.

L'archive ouverte pluridisciplinaire **HAL**, est destinée au dépôt et à la diffusion de documents scientifiques de niveau recherche, publiés ou non, émanant des établissements d'enseignement et de recherche français ou étrangers, des laboratoires publics ou privés.

Earth and Planetary Science Letters 576 (2021) 117171

Contents lists available at ScienceDirect

Earth and Planetary Science Letters

www.elsevier.com/locate/epsl

Seasonal seismic activity on Mars

M. Knapmeyer [a,*], S.C. Stähler [b], I. Daubar [c], F. Forget [d], A. Spiga [d], T. Pierron [d], M. van Driel [b], D. Banfield [e], E. Hauber [a], M. Grott [a], N. Müller [a], C. Perrin [p], A. Jacob [f], A. Lucas [f], B. Knapmeyer-Endrun [g], C. Newman [h], M.P. Panning [i], R.C. Weber [j], F.J. Calef [i], M. Böse [b,r], S. Ceylan [b], C. Charalambous [k], J. Clinton [r], N. Dahmen [b], D. Giardini [b], A. Horleston [l], T. Kawamura [f], A. Khan [b], G. Mainsant [q], M. Plasman [f], M. Lemmon [n], R. Lorenz [o], W.T. Pike [k], J.-R. Scholz [m], P. Lognonné [f], B. Banerdt [i]

[a] *Institute of Planetary Research, DLR, Rutherfordstr. 2, 12489 Berlin, Germany*
[b] *Institute of Geophysics, ETH Zürich, Sonneggstrasse 5, 8092 Zürich, Switzerland*
[c] *Department of Earth, Environmental, and Planetary Sciences, Brown University, Campus Box 1846, Providence, RI 02912-1846, USA*
[d] *Laboratoire de Météorologie Dynamique/Institut Pierre Simon Laplace (LMD/IPSL), Sorbonne Université, Centre National de la Recherche Scientifique (CNRS), École Polytechnique, École Normale Supérieure, France*
[e] *Cornell University, Cornell Center for Astrophysics and Planetary Science, Ithaca, NY, 14853, USA*
[f] *Université de Paris, Institut de physique du globe de Paris, CNRS, F-75005 Paris, France*
[g] *Bensberg Observatory, University of Cologne, Vinzenz-Pallotti-Str. 26, 51429 Bergisch Gladbach, Germany*
[h] *Aeolis Research, 333 N Dobson Road, Unit 5, Chandler, AZ 85224-4412, USA*
[i] *Jet Propulsion Laboratory, California Institute of Technology, 4800 Oak Grove Dr., M/S 183-301, Pasadena, CA 91109, USA*
[j] *NASA MSFC, NSSTC Mail Code ST13, 320 Sparkman Drive, Huntsville, AL 35805, USA*
[k] *Department of Electrical and Electronic Engineering, Imperial College London, South Kensington Campus, London, SW7 2AZ, United Kingdom*
[l] *School of Earth Sciences, University of Bristol, Wills Memorial Building, Queens Road, Bristol BS8 1RJ, United Kingdom*
[m] *Max Planck Institute for Solar System Research, Justus-von-Liebig-Weg 3, 37077 Göttingen, Germany*
[n] *Space Science Institute, 4765 Walnut Street, Suite B, Boulder, CO 80301, USA*
[o] *Johns Hopkins Applied Physics Laboratory, 11100 Johns Hopkins Road, Laurel, MD 20723, USA*
[p] *Laboratoire de Planétologie et Géodynamique, UMR6112, OSUNA UMS3271, Univ. Nantes, Univ. Angers, CNRS, 2 rue de la Houssinière, BP 92208, 44322 Nantes Cedex 3, France*
[q] *Institut Supérieur de l'Aéronautique et de l'Espace SUPAERO, 10 Avenue Edouard Belin, 31400 Toulouse, France*
[r] *Swiss Seismological Service (SED), ETH Zurich, Sonneggstr. 5, 8092 Zurich, Switzerland*

ARTICLE INFO

Article history:
Received 15 February 2021
Received in revised form 9 August 2021
Accepted 12 August 2021
Available online xxxx
Editor: W.B. McKinnon

Dataset link:
https://pds-geosciences.wustl.edu/missions/insight/seis.htm

Dataset link:
https://www.seis-insight.eu/en/science/seis-data/seis-data-description

Dataset link:
https://www.iris.edu/hq/sis/insight

Dataset link: https://atmos.nmsu.edu/data_and_services/atmospheres_data/INSIGHT/insight.html

ABSTRACT

The rate of occurrence of High Frequency (HF) marsquakes, as recorded by InSight at Homestead Hollow, Elysium Planitia, increased after about $L_S = 33°$, and ceased almost completely by $L_S = 187°$, following an apparently seasonal variation with a peak rate near aphelion. We define seismic rate models based on the declination of the Sun, annual solar tides, and the annual CO_2 cycle as measured by atmospheric pressure. Evaluation of Akaike weights and evidence ratios shows that the declination of the Sun is the most likely, and the CO_2 cycle the least likely driver of this seismic activity, although the discrimination is weak, and the occurrence of a few events in August 2020 is in favor for a triggering by CO_2 ice load. We also show that no periodicity related to Phobos' orbit is present in the HF event sequence. Event rate forecasts are presented to allow further discrimination of candidate mechanisms from future observations.

© 2021 The Author(s). Published by Elsevier B.V. This is an open access article under the CC BY-NC-ND license (http://creativecommons.org/licenses/by-nc-nd/4.0/).

* Corresponding author.
E-mail address: martin.knapmeyer@dlr.de (M. Knapmeyer).

https://doi.org/10.1016/j.epsl.2021.117171
0012-821X/© 2021 The Author(s). Published by Elsevier B.V. This is an open access article under the CC BY-NC-ND license (http://creativecommons.org/licenses/by-nc-nd/4.0/).

Dataset link:
https://pds-imaging.jpl.nasa.gov/

Keywords:
Mars
Elysium Planitia
InSight
seasonal seismic activity
Phobos

1. Introduction

NASA's InSight (Interior exploration using Seismic Investigations, Geodesy, and Heat Transport) mission, launched in May 2018, landed in the western part of Elysium Planitia, about 500 km to the north of the dichotomy boundary and 1500 km west of Cerberus Fossae, which was suspected to be seismically active by Taylor et al. (2013). After the touchdown on 26. Nov. 2018, deployment of the seismometer experiment SEIS (Seismic Experiment for Interior Structure; Lognonné et al., 2019, 2020) was completed on sol 70 (the 70th Martian day of the mission). SEIS started continuous recording on sol 73 (09. Feb. 2019), and reached full performance on sol 85 (21. Feb., Banerdt et al., 2020). With the exception of a downtime from 28. Aug. (sol 267) to 18. Sep. 2019 (sol 288, a minor power management problem was extended to three weeks by the 2019 solar conjunction), and a few smaller data losses due to downlink interruptions, SEIS has been recording seismic data continuously ever since.

Estimates of the seismic activity of Mars published prior to the InSight mission basically assumed that marsquakes would occur like earthquakes: according to a Gutenberg-Richter magnitude distribution, and randomly in time (Phillips, 1991; Knapmeyer et al., 2006; Taylor et al., 2013; Plesa et al., 2018, and references therein). A certain class of events, namely High Frequency (HF) and 2.4 Hz events, however, exhibits an occurrence rate that appears variable in time (Giardini et al., 2020), as shown in Fig. 1. HF and 2.4 Hz events are considered jointly here since the latter are small HF events visible only by their excitation of an ambient resonance at 2.4 Hz (Clinton et al., 2021). We interpret the timing of these events as result of a nonstationary Poisson process (supplemental text S7), and compare it with several time-varying processes in order to identify what might drive the nonstationarity. Without even crude epicenter locations, and without knowledge about the current general state of stress - visible faults are millions to billions of years old (Knapmeyer et al., 2006) - a causal stress model to modulate the event rate is not warranted. Our goal is thus to identify a process with a time dependency fitting the event rate, which may inform the identification of candidate source regions: A change of seismicity based on changes of surface load, for example, would point to regions with seasonal ice cover, while a correlation with solar tides would point to the regions with the largest tidal stresses.

Temporal variation of seismic activity is not unheard of. The activity of deep moonquakes is tied to the revolution around the Earth (e.g. Nakamura, 2003; Kawamura et al., 2017), with some source regions being active around perigee or apogee, while others are active at the orbital nodes (Bulow et al., 2007). Short-term temporal variations in lunar impact rate were also detected (Oberst and Nakamura, 1987)

Event rate variations were also described on Earth. Bollinger et al. (2006), for example, conclude that an annual seismicity cycle in Nepal, with a maximum from January to March, is due to the mass loading resulting from the summer monsoon in the Ganges area. At Mt. Hochstaufen, Germany, a strong correlation of seismicity at up to 4.5 km hypocentral depth with rainfall is explained by pore pressure changes in the hectopascal range, which follows rain (Hainzl et al., 2006).

Martian seismicity is certainly not controlled by rainfall, but groundwater pressure might be relevant. Manga et al. (2019) suggest that stresses due to solar tides, Phobos tides, and the diurnal variation of barometric pressure may induce seismic activity by varying aquifer pore pressure beneath a cryospheric ice layer.

The demonstration of a time dependent seismicity on Mars, and of a possible driving force, is impeded by circumstances visible in Fig. 1: Solstices and apsides occur at nearly the same time, i.e. seasonal changes of the weather conditions, especially wind speed, insolation, and atmospheric CO_2 cycle, but also the solar tides all show similar periods and small phase shifts with respect to each other. As reported before by InSight (Lognonné et al., 2020; Giardini et al., 2020; Banfield et al., 2020) and other space craft (Martínez et al., 2017), wind speed varies considerably between day and night, and between seasons, and wind at the landing site is the main source of seismic background noise (Lognonné et al., 2020). It must be shown first that we observe a variation of a seismic source process rather than of detectability. In order to achieve this, a representative subset of all events must be chosen that excludes uncertain detections and possible non-seismic disturbances.

We first describe criteria for the selection of events to evaluate, how we compare a given event rate model with the observed sequence of events, and then discuss a number of simple rate models that are motivated by astronomical or meteorological effects: a noise-dependent detectability of an otherwise constant rate, Phobos tides, impacts, insolation, CO_2 sublimation/deposition, and solar tides. These rate models are then compared and ranked using information theoretical methods.

All mathematical details, including tables coefficients and parameters, and technical details of the grid search for parameter estimation, are presented in the supplementary information, and will be referred to where appropriate (S*n* to refer to supplementary text *n*, and SF*n*, ST*n* for figures or tables).

2. Event selection

We use a preliminary version of the fifth event catalog (InSight Marsquake Service, 2021) covering events that occurred between 12. Jan. 2019 and 31. Aug. 2020. The catalog was published on 04. Jan. 2021, our version was however frozen on 03. Nov. 2020 to have a stable working version. There are no changes from the fourth (InSight Marsquake Service, 2020) to the fifth catalog release concerning HF events, except for quality D event S0568a (02. July 2020). Using the November freeze instead of the public release does thus not affect our results.

The definitions of event categories are given by Clinton et al. (2021, also S2) and are mainly based on the frequency content of signals and, to a lesser extent, other features of the waveforms.

None of the HF events analyzed by van Driel et al. (2021) has a magnitude larger than about 2.2. The events cluster between approx. 20° and 30° distance (van Driel et al., 2021), it was however not possible to locate any of them. Both distances and magnitudes currently depend on assumptions about crustal velocities ($v_S = 2.3$

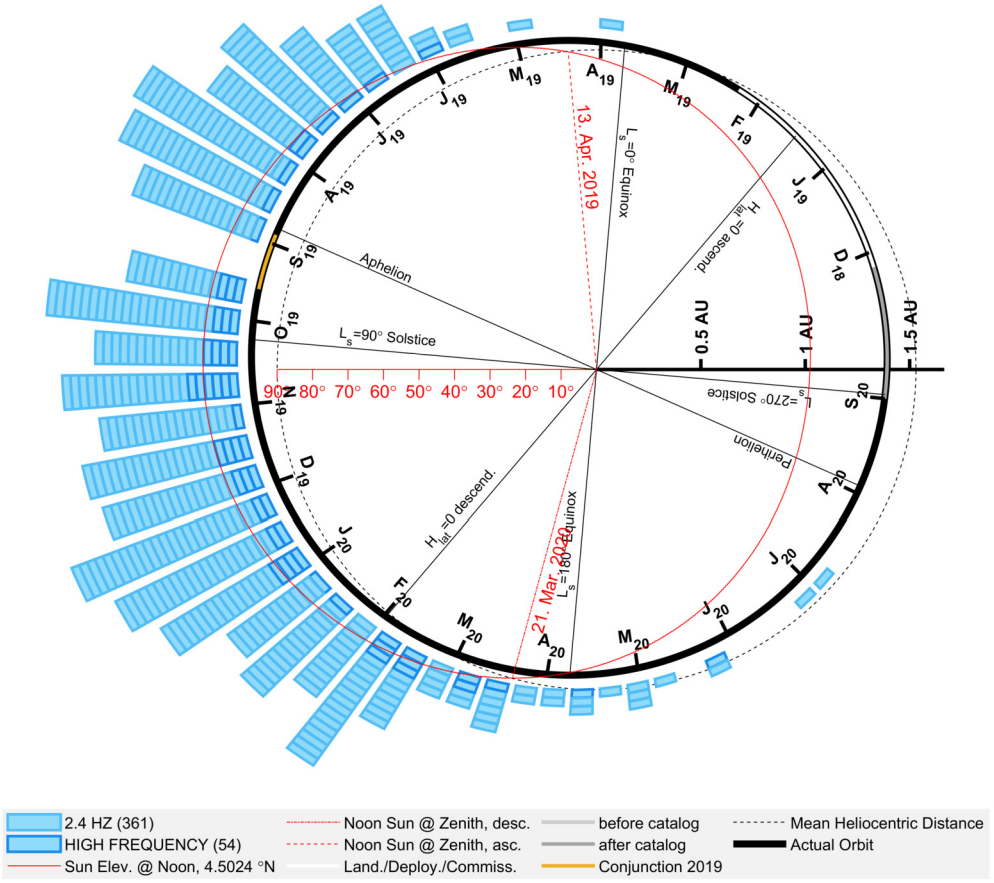

Fig. 1. HF activity over time (all 415 detected events up to 31. Aug. 2020), in relation to the Martian orbit. Rectangular cells indicate the occurrence times of HF events in bins of 5° heliocentric longitude, each rectangle corresponds to one event. High Frequency and 2.4 Hz events are distinguished by edge shading as indicated in the legend. The total event counts for both groups are given in the legend, in brackets. The dashed circle marks the mean orbital radius of Mars (about 1.52 AU), while the heavy ellipse shows the actual orbit, Mars moving counterclockwise (lighter parts indicate times without registration, before and after catalog refers to times before 06. Feb 2019 and after 31. Aug. 2020, as covered by the event catalog used here). Ticks along the orbit denote the beginning of terrestrial months from December 2018 (label D18) until September 2020 (label S20). Equinoxes, solstices, perihelion, aphelion, and zero heliocentric latitude are also marked. The eccentric thin line, and the degrees-scale pointing to the left, indicate the elevation of the sun at noon for the InSight landing site. On 13. Apr. 2019 and 21. Mar 2020, the noonday sun was in the zenith over the InSight lander, and north of InSight in the time between. (For interpretation of the colors in the figure(s), the reader is referred to the web version of this article.)

km/s, $v_P/v_S = 1.7$ in van Driel et al., 2021), where future studies will provide more reliable values.

We focus on the HF family (415 events), but exclude the Very High Frequency events which show a wide distribution of epicentral distances (van Driel et al., 2021), suggesting they are caused by a different process. A future study will deal with the magnitude-frequency distribution and the distribution in time of the Low Frequency and Broadband events (Clinton et al., 2021).

Based on the clarity of seismic arrivals and the degree of polarization, Clinton et al. (2021) define four quality levels "A" (best) to "D" (events that might be artefacts, e.g. wind gusts). We remove all events classified as quality "D" to avoid contamination with non-seismic effects. No HF event is of quality "A".

To cope with limited data transmission volumes, InSight implemented a strategy which includes the buffering of full resolution data on the lander, while only downsampled channels were downlinked continuously (Lognonné et al., 2019). Up to 01. June 2019, continuous data is available at 10 Hz sampling frequency, and at 20 Hz afterwards (see also figure SF1). Data with higher sampling rates are also available for times of identified events prior to 01. June 2020. Although the majority of HF events should be detectable in the 10 Hz data stream, we exclude from our analysis all data that was recorded prior to 01. June 2019.

The most important source of environmental noise is wind. Turbulent winds build up after sunrise and reach speeds of 20 m/s, sometimes more. Around 17:00 LTST, about one hour before sunset, the turbulent flow collapses, and slow laminar winds prevail for several hours (Banfield et al., 2020). Wind speeds increase again after midnight. This has direct consequences for the detection of events, as Giardini et al. (2020) show: 80% of all HF events were detected between 17:00 LTST (Local True Solar Time) and midnight, 15% between midnight and sunrise, and the remaining 5% shortly after sunrise or shortly before 17:00 LTST. The distribution of wind speeds shown by Banfield et al. (2020) mirrors the noise amplitude recorded by SEIS: Figs. 2a and c show the probability density distribution of the noise amplitude, computed as standard deviation of the vertical displacement during 2 min windows, and in relation to a reference displacement of 1 m. These PDFs show the increase of noise during daytime (Fig. 2a and b) as well as its evolution throughout the seasons (Fig. 2b and c).

The events with the smallest recorded displacement amplitudes are most affected by wind noise. The set of selected events should however be representative for the entire population. We therefore exclude from our analysis all events that are recorded with small amplitudes or low signal-to-noise (SNR) ratio (S2 summarizes data processing). To determine acceptance thresholds, we analyze the distributions of amplitudes and SNRs. Fig. 3 shows that the cumulative size-frequency distributions of both amplitudes and SNRs follow a Gutenberg-Richter-like power law. We estimate completeness thresholds for both using the maximum curvature method

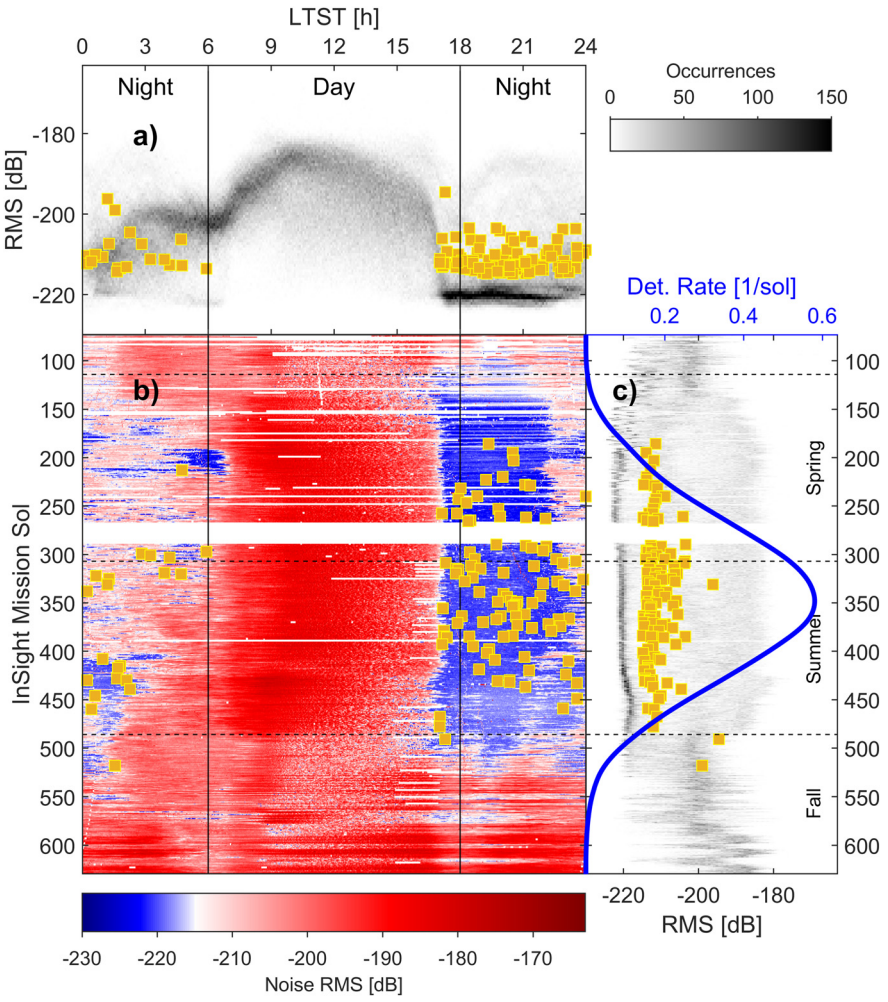

Fig. 2. SEIS background noise and times and amplitudes of the 118 selected events. Noise level is computed as RMS amplitude of vertical displacement between 1.2 Hz and 3.0 Hz, in dB relative to 1 m, and averaged over 2 min windows. Event displacement amplitudes as described in S2. (a) Distribution of noise RMS (2D occurrence count histogram, scaled according to color bar on the right) and event amplitudes (squares) as function of local time LTST. Vertical lines indicate mean sunrise and sunset. (b) Noise RMS amplitude (background color) and event detection times (squares) over time. InSight mission Sol is on the vertical, local time LTST on the horizontal axis. The white point of the color scale is set to the smallest event amplitude (event S0383a, ca. 20:30 LTST, −214.89 dB), such that all events would be detectable at times where the background is blue. Data gaps also map to horizontal white lines. (c) distribution of noise RMS (2D histogram, same scaling and color bar as in (a) and event amplitudes (squares) as function of the InSight mission Sol, dashed horizontal lines indicate beginning of northern seasons. A kernel density estimation of the detection rate is shown in blue (see S3).

(employing kernel density estimation (KDE), see also S4), the distribution slope is obtained as maximum likelihood power law (S4). Based on the results we exclude all events that were recorded with vertical displacement amplitudes below −215 dB, or with an SNR below 2.56. We do not attempt to convert displacement amplitudes into source magnitudes or seismic moments, as this would require better knowledge of epicentral distances than we currently have (cf. van Driel et al., 2021).

With all selection criteria combined, 118 events remain (squares in Fig. 2), of which S0518a is the most recent. These occurred during 458 days (446 sols or 0.67 Martian years). The estimated rate of detection of acceptable events is shown in Fig. 2c (blue), obtained from a kernel density estimation (S3).

3. Inverse problem, parameterization and uncertainties

The problem to solve is to estimate the parameters of a stochastic point process, in the light of a single realization of that process (i.e. the event catalog), requiring a maximum likelihood approach.

If the point process is a non-stationary simple Poisson process (S7), the likelihood L of a candidate rate function is given by (e.g. Ogata, 1983)

$$\log L(\theta) = \sum_{i=1}^{N} \log \lambda(t_i, \theta) - \int_S^T \lambda(u, \theta)\, du \tag{1}$$

(t_i: detection times, λ: rate function, θ: parameter vector, times S and T: beginning and end of observations, respectively). This likelihood is the product of the probability that no event occurs between the observed ones, and the probability of occurrences in an infinitesimal interval after the given times (Ogata, 1983). Multiplication is granted if events are independent. Equation (1) uses the event times directly - it is not necessary to produce any numerical rate estimation based on histograms or kernel densities. Arbitrary, continuously defined candidate rate functions can be compared directly with the event catalog. Lacking epicenters, we approximate source times by arrival times. This introduces 5 to 8 min time errors (van Driel et al., 2021), negligible in comparison to expected rate changes.

We define a generic occurrence rate model, where the actual event rate is the sum of some function of time and a constant baseline rate $\lambda_B \geq 0$, and can never fall below the baseline. Also, the event rate is allowed to lag behind the driving function ac-

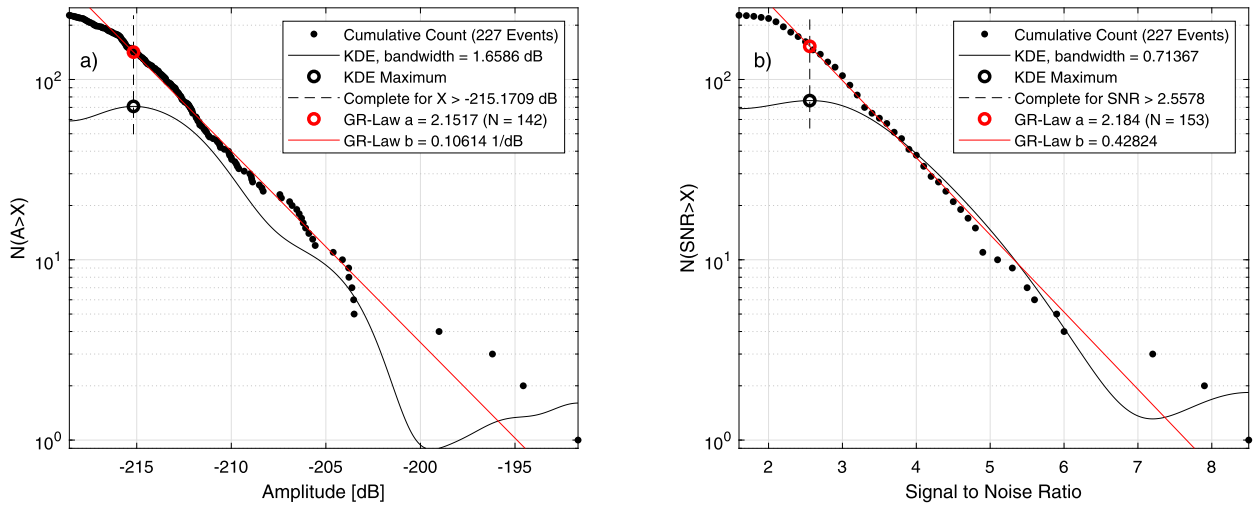

Fig. 3. Event size dependent acceptance thresholds (quality A, B, C events only, 227 events in total): (a) Displacement-Amplitude-frequency distribution, (b) SNR-frequency distribution. Dots represent the observed amplitudes and SNRs, black lines show a kernel density estimation (KDE, with bandwidth as given in the legend) of the respective PDFs (scaled to better comply with the vertical axis range, as only the location of the maximum is important), straight lines show the fitted power law (with completeness threshold a inferred from the KDE, Number N of events above completeness threshold in brackets, and slope b from maximum likelihood estimation, values given in the legends).

cording to a retardation parameter. The detection rate function, as a function of time t and a parameter vector θ, is

$$\lambda\left(t,\theta\right)=\Upsilon\left(t\right)\eta_{det}\left(t\right)\max\left(\lambda_B,f\left(t,\theta_{\setminus\lambda_B}\right)+\lambda_B\right) \tag{2}$$

where f is a model-specific kernel function that depends on time and a parameter vector $\theta_{\setminus\lambda_B}$ (meaning θ without λ_B), and λ_B is the baseline event rate. The function $\Upsilon\left(t\right)$ is 0 during downtimes, 1 else, to describe data gaps (ST2) in the likelihood evaluation. The detection efficiency function $0\leq\eta_{det}\left(t\right)\leq 1$ accounts for the variability of the noise background (see S4 for details).

The maximum likelihood solution θ_{MLE} is obtained from a sequence of nested grid searches (S10). Models with different physical backgrounds are ranked based on Akaike's information criterion (corrected, AICc, S13) and evidence ratios (S14).

The variances of model parameters are given by the inverse Fisher information matrix of the log-likelihood. If this results in negative or extremely large values, we resort to a comparison of likelihoods across the grid and obtain an uncertainty corresponding to $\approx 3\sigma$ (S12).

4. Event rate models

4.1. Can we rule out a constant event rate?

Even if the actual production of events does not vary with time, the strong variation of wind induced noise on SEIS would still result in a parallel variation of the number of event detections per sol. Before comparing event detections with any forcing, it is necessary to demonstrate that a variation exists beyond that expected due to the variable wind noise (i.e. $f\left(t,\theta_{\setminus\lambda_B}\right)\equiv 0$ is the worst kernel). Beyond the qualitative demonstration of Fig. 2, we need a quantitative description.

While it is impossible to know how many events we miss during daytime, we can estimate how many of the events detected at night we would miss if the noise level were higher.

In order to detect events with a displacement of -215 dB with an SNR of 2.56, the noise level must be -223 dB, which is about the lowest observed noise amplitude (Fig. 2). At higher noise levels, the detection rate will be reduced according to the slope of the amplitude-frequency distribution (Fig. 3a) We compute, from noise seismograms and the amplitude distribution slope, a detection efficiency $\eta_{det}\left(t\right)$ which estimates the fraction of events that can be detected at any given time (S4). The difference between the observed cumulative event count and that expected for a stationary Poisson process with detections impeded by the detection efficiency (Fig. 4) then indicates if a significant nonstationary component exists (S5).

In the maximum likelihood analyses of all rate models, we use a polynomial approximation (coefficients in S6) of the empirical detection efficiency function.

As shown in Fig. 4a, the detection rate is almost constant between sol 289 and sol 385; about $67/96=0.698$ events/sol. The thin blue dashed line in Fig. 4a extrapolates the *detection* rate expected for a stationary Poisson process.

Between sol 289 and sol 385, the detection efficiency (red in Fig. 4a) is almost constant at 0.146, implying an *occurrence* rate of 4.78 events/sol. By multiplying this occurrence rate with the time dependent detection efficiency for any time, we obtain the cumulative event count that results from noise level variations (blue solid curve in Fig. 4a). This follows a straight line until about sol 460, when it starts to bend down due to the decreasing detection efficiency, while the observed count starts bending down on sol 385: The observed detection rate starts decreasing before a decrease could be expected from the increasing noise level.

At the time of the last observed event, on sol 518, there is a deficit of 58 events between the observed cumulative count and the straight-line extrapolation, while the deficit between the noise-modulated stationary Poisson process and the straight-line extrapolation is only 18 events: The observed detection rate decreases faster than could be expected from the decreasing detection efficiency. Similar deviations are visible before sol 289.

The observed event sequence is only a single realization of a stochastic process. Individual 446-sols realizations from these processes would however show deviations from the expectation, according to the variance of Poisson processes.

We therefore repeat an analysis like the above for all times at which events were detected, and with a large number of realizations of the simulated noise-modulated stationary Poisson process (see caption of Fig. 4). We compute a residual (observed minus predicted detection count) and calibrate it in terms of the probability that it is smaller than its actual value coincidentally (Fig. 4b).

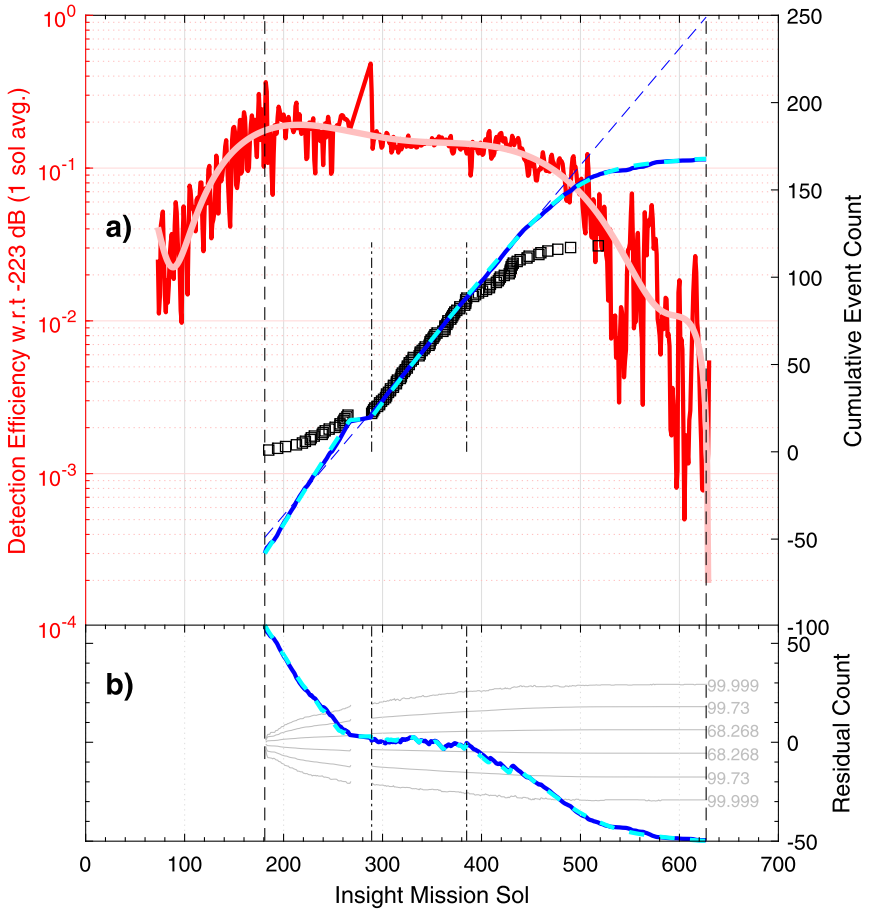

Fig. 4. Nonstationary event rate: (a) Detection efficiency (red curve) relative to a per-sol average noise level of −223 dB, and polynomial fit (pink); Dashed vertical lines: catalog time window. Dash-Dot vertical lines: time window used to estimate the rate of a stationary Poisson process; squares: observed cumulative event count; thin blue dashed line: stationary Poisson process with detection rate 0.698 events/sol (see text); heavy blue solid line: modulation of that process by the actual detection efficiency; heavy blue dashed line: modulation of the same stationary Poisson process by the polynomial fit to the detection efficiency. (b) Residual between observed cumulative count and modulated stationary Poisson processes; thin gray lines: percentiles of the distribution of 10^7 synthetic stationary event sequences that use the rate determined in the time window between dash-dot lines. Percentile values correspond to 1, 3, and 5 standard deviations of a normal distribution.

The probability of accidentally obtaining the observed residual is below 10^{-6} at both ends of the observation time.

For computational efficiency, we use a polynomial approximation (pink in Fig. 4a). Cumulative count and residual are hardly distinct from the empirical curve and residual.

In summary, we have shown that the event detection rate drops too early, too fast, and statistically highly significant. Therefore, a constant event rate is ruled out.

To validate our grid search scheme, we run it with a kernel function

$$f\left(t, \theta_{\setminus \lambda_B}\right) = 0 \tag{3}$$

Using only the events between sols 289 and 385 (parameters in ST11), we find an optimum occurrence rate of 4.63 events/sol ($\log L = -92.97$, $AIC_c = 188$, after 6 iterations), i.e. close to the 4.78 estimated above, while the theoretical values for a rate of 67/96 are $\log L = -91.1$ and $AIC_c = 184.2$ (see S9).

From a grid search using all selected events (ST3), the AICc of the best constant rate is 476.9 (ST17). Any viable time dependent model must have a smaller AICc.

4.2. Are HF events caused by Phobos tides?

We first investigate if the event sequence contains a short period component that could be connected to the groundwater pore pressure effect suggested by Manga et al. (2019).

A spike train Fourier transform (Bulow et al., 2007, S8) does not show any periodicity of event occurrence that can be related to Phobos' orbit. Actually, the power spectral density at Phobos monthly periods (draconitic, anomalistic, synodic) and its culmination period is low compared to the remainder of the analyzed period windows (SF8). The power spectral density shows clear peaks at diurnal and semidiurnal periods. Comparison with synthetic sequences (SF9) lets us attribute the diurnal peak to the low detection probability during daytime. The semidiurnal peak might partially be due to tides, but clearly contains a contribution from the different detection probabilities during the first and second half of the night (SF9). Isolating a solar diurnal or semidiurnal tide signal would require additional effort outside the scope of this paper, which is on longer periods. At this point, we can neither confirm nor exclude the existence of a semidiurnal tidal signal, although we expect that a more dedicated analysis would rather reject it.

We conclude that Phobos did not induce the HF marsquakes studied in this work.

4.3. Are they impacts?

Theoretical models of short-term variations in the impact rate (Ivanov, 2001; JeongAhn and Malhotra, 2015) predict an increased impact rate around aphelion, slightly before the observed seismic activity peak. Although impacts are currently occurring on Mars at

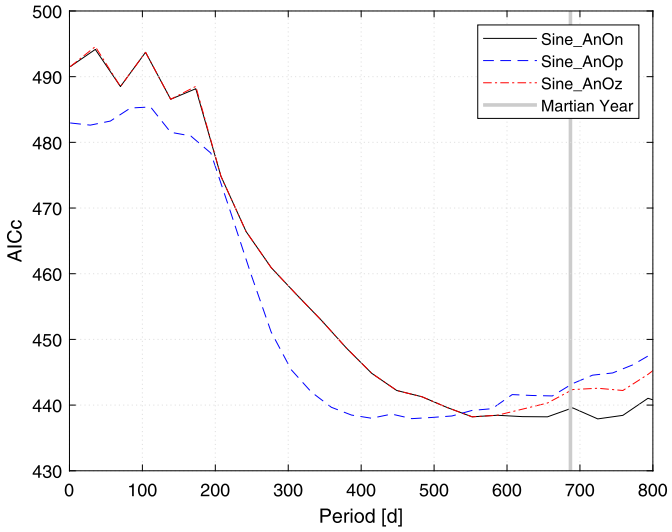

Fig. 5. Lowest AICc values attained for each tested Sine model period (naming conventions: "A" is for amplitude parameter, "O" for offset, "p", "n", "z" denotes positive, negative, or zero values, respectively; the likelihood functions for positive amplitudes are symmetric to those with negative amplitudes when inverting the offset sign). The vertical line indicates an annual period. Since the Sine models used cover different parts of the same parameter space, the existence of minima with the same depth points to the existence of a trade off zone that extends throughout the multidimensional parameter space. With the given data, only periods shorter than 300 days or so can be excluded with some certainty.

a measurable rate (Daubar et al., 2013; Malin et al., 2006), and a fresh crater was found photographically only about 37 km south of InSight, we do not yet have an unambiguous seismic observation of an impact (Daubar et al., 2020). However, attributing the variation in the HF event occurrence rate to impacts would imply that a significant fraction, if not all, of the HF events were in fact impacts. This is also in contradiction with the epicentral distance range of van Driel et al. (2021): Impacts should be distributed uniformly over the planetary surface, and sinusoidal over epicentral distance, with a maximum at $\Delta = 90°$. We do not think that the current observations support an identification of HF events as impacts, so we lay aside the impact hypothesis for now.

4.4. Is there an annual cycle?

The spike train Fourier analysis has no resolution at periods as long as a Martian year yet. Estimating a period length from an observational interval shorter than the expected period clearly involves some extrapolation and can never provide a definitive proof. To test for a periodicity corresponding to that of the Martian year (i.e. $T = 686.9726$ d, S16), we use the simplest periodic kernel function,

$$f(t) = \mathrm{A}\sin(2\pi t/T - \varphi) + K \tag{4}$$

and determine the maximum likelihood period. For eq. (4), the duration of the time windows at which $\lambda(t, \theta) = \lambda_B$ holds, depends on $\sin^{-1} K/A$, thus K is not redundant with λ_B.

We split the parameter space into quadrants of the A-K-plane for reasons of CPU time management. The most likely period found for this kernel is 565 d (550 sols), for $K = 0$. The likelihood maxima identified with nonzero offset are at both shorter and longer periods, inspection of the search grids however shows that the period is poorly resolved (Fig. 5). The AICc as function of period shows a trough that shifts toward longer periods as the Offset parameter becomes smaller and negative, suggesting the existence of a tradeoff between Offset and other parameters. The common envelope of all curves in Fig. 5 shows that the assumed period can be varied over a wide range without increasing the AICc. The standard deviations obtained analytically and from comparing likelihood values across the grid are either infinite or encompass the entire search grid (ST15, ST16), indicating that a reliable determination of the period is not yet possible. This evaluation nevertheless supports that there is no significantly shorter period involved.

This analysis neither proves nor disproves the existence of an annual cycle. Strictly spoken, we can also not exclude the possibility that we witnessed a singular burst of activity, unless the activity actually repeats. But since annual periods are plausible and not prohibited, we investigate several mechanisms which imply an annual period.

4.5. Illumination model

The Sun's elevation above the equator is described by $\sin L_S(t)$ (S15), where L_S is the areocentric longitude of the Sun commonly used to define Martian seasons (S16). By a small modification of eq. (4) we thus obtain the illumination model

$$f(t) = \mathrm{A}\sin(L_s(JD_{TT} - D)) + K \tag{5}$$

as kernel function, where time is measured as Julian Date JD_{TT} (index TT for terrestrial time, i.e. no leap seconds are introduced), and retardation is defined as a time delay D in days.

4.6. Surface load model

Induced seismicity is known on Earth from water level changes in reservoirs, caused by pore pressure changes at depth that follow the load change (Bell and Nur, 1978). The phase lag between infill change and seismicity can even exceed 180° (Roeloffs, 1988). Besides reservoir mass, the water level change rate is one of the key parameters that control the temporal distribution of induced seismicity (Saxena et al., 1988). As the polar caps of Mars are known to show a seasonal deposition/evaporation cycle since Herschel (1784), we investigate the possibility of changing CO_2 ice load as driver for the HF seasonality. A discussion of the involved atmospheric pressure changes and mass movements is provided in S12.

Since the surface load from CO_2 deposition increases when atmospheric pressure decreases, we use a kernel function based on the negative of the pressure change. The time derivative of $dP(L_S(t))/dt$ also involves the time derivative of $L_S(t)$ (S17). The kernel function is

$$f(t) = A(-dP(L_S(JD_{TT} - D))/dt) + K \tag{6}$$

with parameters analogous to the illumination model.

4.7. Annual solar tide

Seismic activity of the Moon is mainly due to Earth's tides (Bulow et al., 2007). Earthquakes triggered by lunar tides have been reported (e.g. Rydelek et al., 1988), but are overwhelmed by plate tectonic background activity: only about one percent of midcrustal seismicity is related to tides (Lockner and Beeler, 1999; Métivier et al., 2009). We are not aware of any study of earthquakes related to solar tides, but as these are weaker than lunar tides, earthquakes due to solar tides will be even more difficult to identify.

We ruled out diurnal Phobos tides as reason for HF marsquakes above, while the daily wind speed pattern makes solar diurnal tides inaccessible for our analysis. Phillips (1991) concluded that the annual solar tide does not contribute to Martian seismicity,

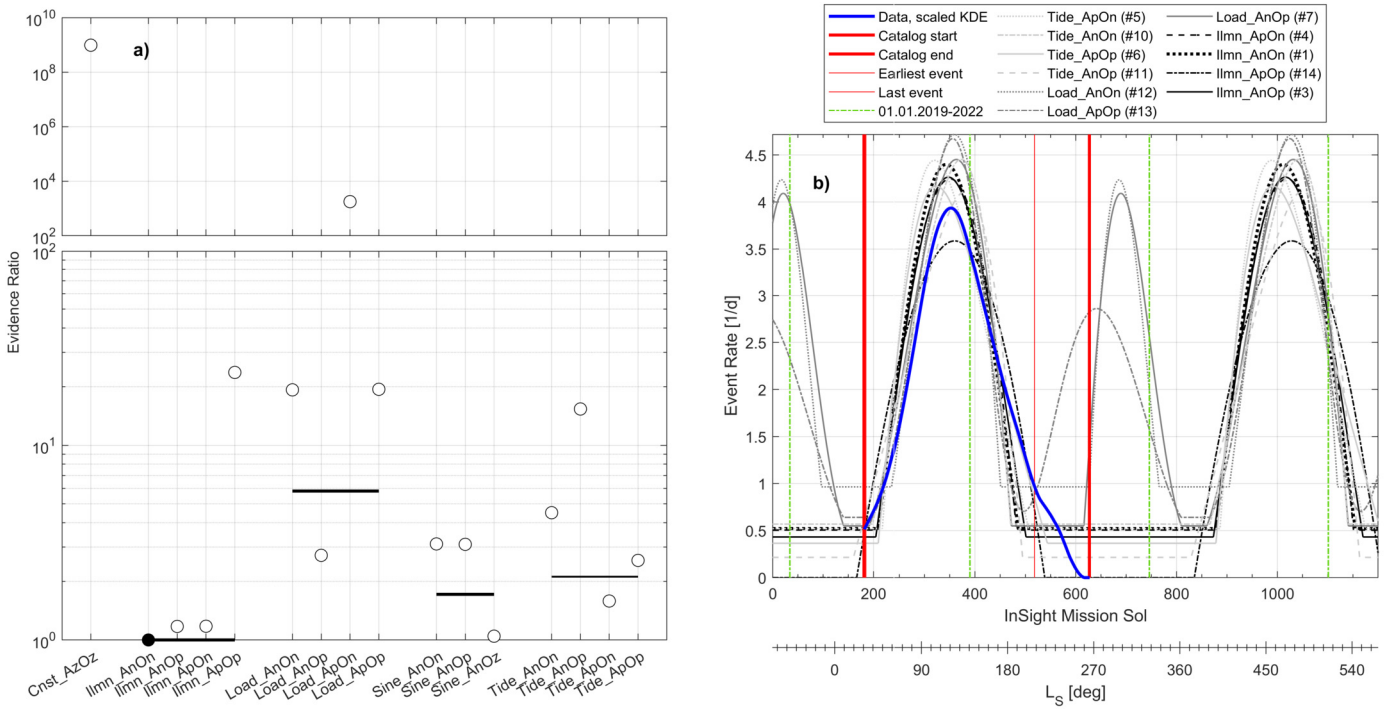

Fig. 6. Evidence ratios and rate forecasts. a) Evidence ratios for individual models and model groups (numerical values in table ST17). Filled circle: most supported model, open circles: evidence ratios with respect to the most supported model ($\mathcal{R}_{best} = 1$), black bars: evidence ratios of model groups with respect to the most supported group. A marker at a ratio $\mathcal{R}$ means that the model or group at $\mathcal{R}_{best} = 1$ is $\mathcal{R}$ times more likely to be the truly best model or group than the one with $\mathcal{R}_i = \mathcal{R}$. The lower part of the diagram is a continuation of the upper part, with higher vertical resolution. b) Rate forecast until sol 1200 (12. Apr. 2022) for models with $\mathcal{R}_i < 100$ (excluding Sine models, numbers in legend indicate evidence ranking). Vertical lines mark the time covered by observations (solid; catalog start and 1st event coincide) and the terrestrial calendar year (dash-dot lines for 1. Jan, starting 2019). A kernel density estimation (heavy solid curve with a bump between sols 500 and 600) illustrates the observed event rate but is not used during the inversion. The secondary x axis gives the areocentric solar longitude L_S corresponding to the mission sols, see Fig. 2b for the relation to martian seasons.

since absolute strain is low, although strain rates are high, compared to other sources of deformation. In contrast, Manga et al. (2019) conclude that an annual variation of seismic activity due to the ellipticity of the Martian orbit is well possible. With the observations of InSight, it now becomes possible to challenge both views.

Although Manga et al. (2019) provide a detailed framework for the modification of seismicity due to volumetric strain and resulting changes of pore pressure in the crust, we continue to use our rate function approach. An evaluation of deformation and stress tensors, and the dependency of phase lag on fault orientation, would require more knowledge of the seismic sources and their location than we currently have. Instead, we define a time dependency in terms of the radial tidal displacement. The resulting radial strain rate is proportional to $\dot{R}(t)/R^4(t)$, where $R(t)$ is the heliocentric distance of Mars (S20). We use a truncated series approximation of this distance and its derivative (S20) to capture the time dependency, but leave aside scaling parameters like masses and Newton's constant of gravity when we define the kernel function

$$f(t) = A\dot{R}(JD_{TT} - D)/\left(R_0^3 R^4(JD_{TT} - D)\right) + K \tag{7}$$

with parameters analogous to the illumination and surface load models, and R_0 being the mean distance between Mars and Sun in astronomical units.

5. Solutions and forecasts

From the model types described above, we define a total of 16 distinct models, which either use different kernel functions ("Cnst", "Ilmn", "Load", "Sine", or "Tide"), or are restricted to certain parameter ranges. After test runs, we decided to investigate positive and negative values of amplitude factors and constant kernel offsets separately, to avoid convergence to local maxima. We append an "A" and an "O", followed by "n", "p", or "z", respectively, to indicate if amplitude and offset are negative, positive, or zero.

With a collection of models that imply different physical effects at the source of the HF events, we not only have to ask which values of the model parameters are most likely, but which model is the most likely one, in the light of stochastic point process data. An appropriate framework is the concept of Kullback-Leibler information (Kullback and Leibler, 1951), which allows asking how much information is lost when the data is described by a model instead of the unknown real processes. From the maximum likelihood solution, we compute the Akaike Information Criterion with bias correction (AICc) and use Akaike weights and evidence ratios $\mathcal{R}_i$ between models (S13, S14).

The evidence ratios account for the sampling uncertainty of the computed AICc values (S11, ST16, ST17) and indicate how much more likely the preferred model is actually the best choice, rather than just appearing so by chance due to the limited data. Since our models form groups according to the rate kernels used, we also compute evidence ratios for these groups (Fig. 6a). For comparison, Fig. 6b also shows a kernel density estimation (KDE) of the observed rate function.

It is not surprising that the evidence speaks clearly (i.e. with a high evidence ratio) against the constant-rate model Cnst_AzOz, since the obvious deviation from a constant rate was what triggered our study, demonstrated above.

The preferred model is Ilmn_AnOn. The second-best model is Sine_AnOz. The group of Ilmn-models is actually the best group, while the group of Sine models comes second.

The Sine models, however, have no physical background but were introduced only to test the plausibility of an annual periodicity. Inspection of the coefficients in the series expansion of $L_S(t)$ (ST6) shows that $L_S(t)$ is dominated by the $i = 0$ term, i.e. $L_S(t) \propto t$ can be considered as first order approximation, and hence the Sine models perform so well because they are a good approximation to the Illumination model. The Sine models are thus redundant with the Illumination models and are not considered any further. This leaves us with the annual solar tide models as the second-best model group, while the surface load models come third. The best individual tide model Tide_ApOn is also the 2nd best physical model in total. Only three of the surface load models are supported by the data: the variants with negative offset are ruled out by evidence ratios exceeding $\mathcal{R} > 10^3$, compared to $\mathcal{R} < 20$ for positive offsets.

We examine closer models with evidence ratio below 100, i.e. the 11 best models (Fig. 6b).

Their effective amplitude at the time of the activity maximum is 3.5 to 4.5 events per day, about the observed rate after correction for detection efficiency. The baseline rate is about 0.5 events/day in most cases, and thus considerably below the maximum rate.

The lags of the models vary largely: event activity lags behind the driving function by 393 d for #1 ranked model Ilmn_AnOn, but only by 44 d for Ilmn_ApOn. If the illumination affects seismic activity by heating the ground, even the higher value points to a very shallow source, as the annual heat wave is expected to penetrate only a few meters (Siegler et al., 2017). More indirect triggering mechanisms, e.g. via a pore pressure reduction after a fluid release in a gully, might have an effect to greater depth, similar to the rain at Mt. Hochstaufen (Hainzl et al., 2006). The tide models show lags of either about 280 d or about 575 d.

The load model lags are either around 16 d or around 500 d: For the best load model, Load_AnOp, the time lag is 18.4 d (17.9 sols). This means that the seismicity maximum of sol 352 (22. Nov. 2019, $L_S = 110°$, see Fig. 6b) is the response to the pressure change in early November 2019 ($L_S = 102°$), which is the time of the largest pressure decrease (SF11). With a negative amplitude factor (ST15) this corresponds to the fastest ice deposition (on global average). Likewise, a lag time of about 494 or 507 d (Load_ApOn, Load_ApOp) points to late June or early July 2018 ($L_S \approx 200°$), when pressure increase was near maximum. With a positive amplitude factor, this corresponds to an increasing ice load as well.

It might be useful to consider periods longer than half a year as negative lags in the case of tidal models, and connect them to tidal dissipation models to further down-select the models.

We forecast the HF event rate for two Martian years following deployment completion (Fig. 6b). All models agree that an activity phase comparable to that observed so far will repeat in basically identical form from April 2021 (sol 840 in Fig. 6b) to March or April 2022 (sol 1150 and later), with an activity maximum between September and November 2021 (approx. sol 990 to 1050, precise dates in ST18). Two surface load models in this selection however forecast an earlier resume of activity, starting already from early spring 2020 (sol 496 for model Load_ApOp), with an activity maximum in fall 2020 (between sol 641 for Load_ApOp, and sol 689 for Load_AnOp), and lasting until March 2021 (around sol 810).

An interesting detail is the slight increase of the kernel density rate estimation after Sol 528 (21. May 2020, KDE in Fig. 6b), which approximately coincides with the second activity maximum predicted by the Load_ApOp model. Load_ApOp is the only model showing an event rate above its baseline rate at this time (see also SF15). In May 2020 ($L_S = 205°$), the noise level was already increased (Fig. 2) and the detection efficiency reduced (Fig. 4), thus only a small number of detections could be expected irrespective of the driving force. This result is in contradiction with the expected absence of CO_2 ice in the vicinity of InSight, but, with the small number of involved events, it does also not prove much. An unambiguous (non-) observation of the additional activity maxima predicted by the ice load models would be strong evidence for (or against) them. Among the models with evidence ratio below 100, Load_ApOp is however the second worst (evidence ratio 19.3). Without more data from this part of the activity cycle (if it is a cycle) it is difficult to tell how important this detail in the KDE rate estimation really is. The differences in the times predicted above only account for the differences between the model types, but not for the uncertainty of model parameters. The time intervals given so far are therefore likely to underestimate the actual uncertainty of begin, maximum, and end times. Unfortunately, the determination of parameter uncertainties using the Fisher information matrix failed for the preferred model, and also for several other models, such that we have to resort to the Jackknife approach (results in ST16).

For Ilmn_AnOn we find a standard deviation of the likelihood $\sigma_{MLE} = 6.36$ ($\log L_{MLE} = -213.57$, ST16, ST17). To estimate the uncertainty of the forecasts made above, we consider all parameters with likelihoods less than one standard deviation below the maximum. For these models, the beginning of the next activity phase varies from sol 853 (20. Apr. 2021) to sol 918 (26. June 2021), and the time of the next maximum is between sol 997 (15. Sep. 2021) and sol 1045 (03. Nov. 2021) (SF16). The expected number of events is as in the previous maximum. This timing uncertainty basically covers the variability between the individual models shown in Fig. 6b (except for the additional maxima of the load models).

For model Load_ApOp ($\log L_{MLE} = -216.7$), we obtain $\sigma_{MLE} = 6.19$ and again inspect models with likelihoods less than one standard deviation below the maximum (SF17). We find two distinct solutions for the timing of the additional activity phase, with maxima between sol 608 (11. Aug. 2020) and sol 738 (23. Dec. 2020), and a third maximum between sol 976 (25. Aug. 2021) and sol 1040 (28. Oct. 2021) and event rates similar to those experienced so far. In most cases, however, the rate never decreases to 0, with a minimum rate between sol 828 (25. Mar. 2021) and sol 880 (18. May 2021) (SF17). The expected event rate for the December 2020 maximum is about half the previous maximum. In general, these models alternate between two maximum rates, i.e. a higher maximum is followed by a lower one and vice versa.

For model Load_AnOp ($\log L_{MLE} = -214.6$) we obtain $\sigma_{MLE} = 6.32$, models within one standard deviation of the maximum likelihood solution are collected in figure SF19. Like Load_ApOp, this model also forecasts two phases of activity per year. One maximum is expected between sol 668 (12. Oct. 2020) and sol 719 (03. Dec. 2020). A phase with minimum or constant background activity might follow between sol 752 (06. Jan. 2021) and sol 862 (29. Apr. 2021), and another activity maximum is forecast to occur between sol 994 (12. Sep. 2021) and sol 1062 (21. Nov. 2021). The event rate at both the maxima is expected to be similar to the previous maximum.

6. Conclusions

We analyzed the High Frequency family of events detected by InSight on Mars, while we left out the Very High Frequency, Low Frequency and Broadband events which all appear to be of a different origin (Giardini et al., 2020; Clinton et al., 2021; van Driel et al., 2021).

We tested time variable event rate functions based on five different driving effects. Two of them (Phobos tides and impacts) were excluded from further analysis in an early stage, for the other three models (elevation of the Sun, seasonal surface loads, and solar tides) we conducted a maximum likelihood analysis and provide an Akaike weight-based ranking.

The evidence ratios between our three groups of models, and the 16 individual models within those groups, are not fully conclusive yet. One challenge is the coincidental proximity of the solstices to aphelion and perihelion. A higher resolution of activity levels and durations is required in order to discern tidal and climate forcing. This may be achieved in the future by stacking activity observations from more than one Martian year. Any of the models may still fail when future observations are compared to its activity forecasts, hence an extended observation would help discriminate between models. At least observing a second cycle would be necessary to rule out that we just witnessed a singular, non-recurring burst of activity.

The best ranked rate model is the seasonal change of illumination, followed by annual solar tides and changing CO_2 ice load, in that order. There are indications of an additional activity maximum which could only be explained by the ice load model, though.

The physical mechanism for how illumination is connected to the HF marsquake sources remains to be determined. While thermal shocking is a known agent of weathering (e.g. Hall and Thorn, 2014), the penetration depth of the diurnal heat wave, and the amount of material mobilized in each cycle, are small (e.g. Lamp et al., 2017). In addition, landslides are inefficient seismic sources, which require enormous amounts of mass moved to obtain a seismic signal that can be recorded over long distances (e.g. Berrocal et al., 1978; Deparis et al., 2008), especially when accounting for the Martian environment (Lucas et al., 2019). Assuming falling boulders in Cerberus Fossae as source, for example, would imply erosion rates which probably do not agree with the crisp topography of its deep, narrow valleys. Recent avalanches on the northern polar cap, captured by HiRise on 29. May 2019 (Image ESP_060176_2640), were not detected by InSight.

Gullies are known to show a seasonal activity as well (Dundas et al., 2012), but are found only at latitudes beyond 30°, some however within less than 35° distance from InSight (Conway et al., 2019a,b). If gully activity is due to more or less deep aquifers (as suggested by Heldmann et al., 2007), aquifer pore pressure might be a crucial parameter. It is however unclear if this is the case, or if gaseous CO_2 plays a major role, while the absence of CO_2 in terrestrial analogs limits our understanding (see recent reviews of Conway et al., 2019a,b, and Dundas et al., 2019).

The CO_2 ice load model, as used here, reflects global-scale deposition and evaporation, but is mainly driven by the polar ice caps. These, however, are farther away from InSight than travel time analysis of the HF events allows the source to be. The assumption of a circumpolar origin would require very high seismic velocities even in the upper mantle and would be more difficult to reconcile with the coda present in HF seismograms, which suggest wave propagation dominantly through the crust (Giardini et al., 2020; van Driel et al., 2021). The lower latitude CO_2 deposits mentioned before are smaller in volume, and may condensate and evaporate with shorter time constants than the larger polar deposits. Also, especially the evaporation is certainly not independent from insolation, and the respective rate models are not as independent of each other as one would like them to be for a clear discrimination. Improved time dependency models for low-latitude ice deposits may help to disentangle the rate models.

We have shown that the annual variation of wind noise is not sufficient to explain the annual variability of HF event detections - they really occur at a variable rate. Our study suggests that, once the epicenters of HF sources can be better constrained, we should inspect regions where topography causes strong seasonal insolation variations, or where CO_2 ice is deposited in the cold times of the year, for indications of macroseismic changes due to the "marsquake season".

CRediT authorship contribution statement

M. Knapmeyer: Conceptualization, Formal analysis, Methodology, Software, Validation, Visualization, Writing – original draft, Writing – review & editing. **S.C. Stähler:** Conceptualization, Data curation, Software, Visualization, Writing – review & editing. **I. Daubar:** Writing – original draft. **F. Forget:** Data curation, Formal analysis, Methodology, Writing – original draft. **A. Spiga:** Data curation, Formal analysis, Methodology, Writing – original draft. **T. Pierron:** Formal analysis, Methodology, Writing – original draft. **M. van Driel:** Conceptualization, Data curation. **D. Banfield:** Data curation. **E. Hauber:** Conceptualization. **M. Grott:** Conceptualization. **N. Müller:** Conceptualization. **C. Perrin:** Conceptualization, Data curation. **A. Jacob:** Conceptualization. **A. Lucas:** Conceptualization. **B. Knapmeyer-Endrun:** Conceptualization, Data curation. **C. Newman:** Conceptualization. **M.P. Panning:** Funding acquisition, Project administration, Writing – review & editing. **R.C. Weber:** Conceptualization, Writing – review & editing. **F.J. Calef:** Writing – original draft. **M. Böse:** Data curation, Formal analysis, Investigation. **S. Ceylan:** Data curation, Formal analysis, Investigation. **C. Charalambous:** Data curation, Formal analysis, Investigation. **J. Clinton:** Data curation, Formal analysis, Investigation. **N. Dahmen:** Data curation, Formal analysis, Investigation. **D. Giardini:** Funding acquisition, Project administration. **A. Horleston:** Data curation, Formal analysis, Investigation. **T. Kawamura:** Data curation, Formal analysis, Investigation. **A. Khan:** Data curation, Formal analysis, Investigation. **G. Mainsant:** Data curation, Formal analysis, Investigation. **M. Plasman:** Data curation, Formal analysis, Investigation. **M. Lemmon:** Writing – review & editing. **R. Lorenz:** Writing – review & editing. **W.T. Pike:** Funding acquisition, Project administration. **J.-R. Scholz:** Data curation, Formal analysis, Investigation. **P. Lognonné:** Data curation, Funding acquisition, Investigation, Project administration. **B. Banerdt:** Funding acquisition, Project administration.

Declaration of competing interest

The authors declare that they have no known competing financial interests or personal relationships that could have appeared to influence the work reported in this paper.

Data availability

All SEIS data are available in SEED format (InSight Mars SEIS Service, 2019a) or PDS4 format (InSight Mars SEIS Service, 2019b). Events used in this analysis are listed in the MQS catalogue (InSight Marsquake Service, 2020, 2021). Noise RMS amplitudes and event catalog are based on waveform data which is released to the public via the NASA Planetary Data System (https://pds-geosciences.wustl.edu/missions/insight/seis.htm), IPGP Data center (https://www.seis-insight.eu/en/science/seis-data/seis-data-description) and IRIS DMC (https://www.iris.edu/hq/sis/insight) several times a year.

Data from the APSS pressure sensor and the temperature and wind (TWINS) sensor referenced in this paper are available from the PDS Atmospheres node. The direct link to the InSight data archive at the PDS Atmospheres node is https://atmos.nmsu.edu/data_and_services/atmospheres_data/INSIGHT/insight.html.

Images from the Mars Reconnaissance Orbiter camera HiRise are stored in the NASA Planetary Data System at https://pds-imaging.jpl.nasa.gov/.

Acknowledgements

We are grateful to Peter Shearer and an anonymous reviewer, whose comments helped to improve the manuscript.

We acknowledge NASA, CNES, partner agencies and Institutions (UKSA, SSO, DLR, JPL, IPGP-CNRS, ETHZ, IC, MPS-MPG) and the operators of JPL, SISMOC, MSDS, IRIS-DMC and PDS for providing SEED SEIS data.

I.J.D. is supported by NASA InSight Participating Scientist grant 80NSSC20K0971.

This is Insight contribution ICN185.

Appendix A. Supplementary material

Supplementary material related to this article can be found online at https://doi.org/10.1016/j.epsl.2021.117171.

References

Banerdt, W.B., Smrekar, S.E., Banfield, D., Giardini, D., Golombek, M., Johnson, C.L., Lognonné, P., Spiga, A., Spohn, T., Perrin, C., Stähler, S.C., Antonangeli, D., Asmar, S., Beghein, C., Bowles, N., Bozdag, N., Chi, P., Christensen, U., Clinton, J., Collins, G.S., Daubar, I., Dehant, V., Drilleau, M., Fillingim, M., Folkner, W., Garcia, R.F., Garvin, J., Grant, J., Grott, M., Grygorczuk, J., Hudson, T., Irving, J.C.E., Kargl, G., Kawamura, T., Kedar, S., King, S., Knapmeyer-Endrun, B., Knapmeyer, M., Lemmon, M., Lorenz, R., Maki, J.N., Margerin, L., McLennan, S.M., Michaut, C., Mimoun, D., Mittelholz, A., Mocquet, A., Morgan, P., Mueller, N.T., Murdoch, N., Nagihara, S., Newman, C., Nimmo, F., Panning, M., Pike, W.T., Plesa, A.-C., Rodriguez, S., Rodriguez-Manfredi, J.A., Russell, C.T., Schmerr, N., Siegler, M., Stanley, S., Stutzmann, E., Teanby, N., Tromp, J., van Driel, M., Warner, N., Weber, R., Wieczorek, M., 2020. Initial results from the InSight mission on Mars. Nat. Geosci. 13, 183–189. https://doi.org/10.1038/s41561-020-0544-y.

Banfield, D., Spiga, A., Newman, C., Forget, F., Lemmon, M., Lorenz, R., Murdoch, N., Viudez-Moreiras, D., Pla-Garcia, J., Garcia, R.F., Lognonné, P., Karatekin, Ö., Perrin, C., Martire, L., Teanby, N., van Hove, B., Maki, J., Kenda, B., Mueller, N.T., Rodriguez, S., Kawamura, T., McClean, J.B., Stott, A.E., Charalambous, C., Millour, E., Johnson, C.L., Mittelholz, A., Määttänen, A., Lewis, S.R., Clinton, J., Stähler, S.C., Ceylan, S., Giardini, D., Warren, T., Pike, T., Daubar, I., Golombek, M., Rolland, L., Widmer-Schnidrig, R., Mimoun, D., Beucler, É., Jacob, A., Lucas, A., Baker, M., Ansan, V., Hurst, K., Mora-Sotomayor, L., Navarro, S., Torres, J., Lepinette, A., Molina, A., Marin-Jimenez, M., Gomez-Elvira, J., Peinado, V., Rodriguez-Manfredi, J.-A., Carcich, B.T., Sackett, S., Russell, C.T., Spohn, T., Smrekar, S.E., Banerdt, W.B., 2020. The atmosphere of Mars as observed by InSight. Nat. Geosci. 13, 190–198. https://doi.org/10.1038/s41561-020-0534-0.

Bell, M.L., Nur, A., 1978. Strength changes due to reservoir-induced pore pressure and stresses and application to Lake Oroville. J. Geophys. Res. 83 (B9), 4469–4483.

Berrocal, J., Espinosa, A.F., Galdos, J., 1978. Seismological and geological aspects of the Mantaro landslide in Peru. Nature 275, 533–536.

Bollinger, L., Perrier, F., Avouac, J.-P., Sapkota, S., Gautam, U., Tiwari, D.R., 2006. Seasonal modulation of seismicity in the Himalaya of Nepal. Geophys. Res. Lett. 34, L08304. https://doi.org/10.1029/2006GL029192.

Bulow, R.C., Johnson, C.L., Bills, B.G., Shearer, P.M., 2007. Temporal and spatial properties of some deep moonquake clusters. J. Geophys. Res. 112, E09003. https://doi.org/10.1029/2006JE002847.

Clinton, J.F., Ceylan, S., van Driel, M., Giardini, D., Stähler, S.C., Böse, M., Charalambous, C., Dahmen, N.L., Horleston, A., Kawamura, T., Khan, A., Orhand-Mainsant, G., Scholz, J.-R., Euchner, F., Banerdt, W.B., Lognonné, P., Banfield, D., Beucler, E., Garcia, R.F., Kedar, S., Panning, M.P., Perrin, C., Pike, W.T., Smrekar, S.E., Spiga, A., Stott, A., 2021. The Marsquake catalogue from InSight, sols 0–478. Phys. Earth Planet. Inter. 310. https://doi.org/10.1016/j.pepi.2020.106595.

Conway, S., de Haas, T., Harrison, T., 2019a. Martian gullies: a comprehensive review of observations, mechanisms and insights from Earth analogues. In: Conway, S.J., Carrivick, J.L., Carling, P.A., de Haas, T., Harrison, T.N. (Eds.), Martian Gullies and Their Earth Analogues. Geol. Soc. (Lond.) Spec. Publ. 467, 7–66. https://doi.org/10.1144/SP467.14.

Conway, S., Harrison, T., Soare, R., Britton, A., Steele, L., 2019b. New slope-normalised global gully density and orientation maps for Mars. Geol. Soc. (Lond.) Spec. Publ. 467 (1), 187–197. https://doi.org/10.1144/SP467.3. Geological Society of London. hal-02270628ff.

Daubar, I.J., McEwen, A.S., Byrne, S., Kennedy, M.R., Ivanov, B.A., 2013. The current martian cratering rate. Icarus 225, 506–516. https://doi.org/10.1016/j.icarus.2013.04.009.

Daubar, I.J., Lognonné, P., Teanby, N.A., Collins, G.S., Clinton, J., Stähler, S., Spiga, A., Karakostas, F., Ceylan, S., Malin, M., McEwen, A.S., Maguire, R., Charalambous, C., Onodera, K., Lucas, A., Rolland, L., Vaubaillon, J., Kawamura, T., Böse, M., Horleston, A., van Driel, M., Stevanović, J., Miljković, K., Fernando, B., Huang, Q., Giardini, D., Larmat, C.S., Leng, K., Rajšić, A., Schmerr, N., Wójcicka, N., Pike, T., Wookey, J., Rodriguez, S., Garcia, R., Banks, M.E., Margerin, L., Posiolova, L., Banerdt, B., 2020. A new crater near InSight: implications for seismic impact detectability on Mars. J. Geophys. Res., Planets 125 (8). https://doi.org/10.1029/2020JE006382.

Deparis, J., Jongmans, D., Cotton, F., Baillet, L., Thouvenot, F., Hantz, D., 2008. Analysis of rock-fall and rock-fall avalanche seismograms in the French Alps. Bull. Seismol. Soc. Am. 98 (4), 1781–1796. https://doi.org/10.1785/0120070082.

Dundas, C.M., Diniega, S., Hansen, C.J., Byrne, S., McEwen, A.S., 2012. Seasonal activity and morphological changes in Martian gullies. Icarus 220, 124–143. https://doi.org/10.1016/j.icarus.2012.04.005.

Dundas, C.M., McEwen, A.S., Diniega, S., Hansen, C.J., Byrne, S., McElwaine, J.N., 2019. The formation of gullies on Mars today. In: Conway, S.J., Carrivick, J.L., Carling, P.A., de Haas, T., Harrison, T.N. (Eds.), Martian Gullies and Their Earth Analogues. Geol. Soc. (Lond.) Spec. Publ. 467, 67–94. https://doi.org/10.1144/SP467.5.

Giardini, D., Lognonné, P., Banerdt, W., Pike, W., Christensen, U., Ceylan, S., Clinton, J., van Driel, M., Stähler, S., Böse, M., Garcia, R.F., Khan, A., Panning, M., Perrin, C., Bandfield, D., Beucler, E., Charalambous, C., Euchner, F., Horleston, A., Jacob, A., Kawamura, T., Kedar, S., Mainsant, G., Scholz, J.-R., Smrekar, S., Spiga, A., Agard, C., Antonangeli, D., Barkaoui, S., Barrett, E., Combers, P., Conejero, V., Daubar, I., Drilleau, M., Ferrier, C., Gabsi, T., Gudkova, T., Hurst, K., Karakostas, F., King, S., Knapmeyer, M., Knapmeyer-Endrun, B., Llorca-Cejudo, R., Lucas, A., Luno, L., Margerin, L., McClean, J., Mimoun, D., Murdoch, N., Nimmo, F., Nonon, M., Pardo, C., Rivoldini, A., Rodriguez Manfredi, J.A., Samuel, H., Schimmel, M., Stott, A.E., Stutzmann, E., Teanby, N., Warren, T., Weber, R., Wieczorek, M., Yana, C., 2020. The seismicity of Mars. Nat. Geosci. 13, 205–212. https://doi.org/10.1038/s41561-020-0539-8.

Hainzl, S., Kraft, T., Wassermann, J., Igel, H., Schmedes, E., 2006. Evidence for rainfall-triggered earthquake activity. Geophys. Res. Lett. 33, L19303. https://doi.org/10.1029/2006GL027642.

Hall, K., Thorn, C.E., 2014. Thermal fatigue and thermal shock in bedrock: an attempt to unravel the geomorphic processes and products. Geomorphology 206, 1–13. https://doi.org/10.1016/j.geomorph.2013.09.022.

Heldmann, J.L., Carlsson, E., Johansson, H., Mellon, M.T., Toon, O.B., 2007. Observations of Martian gullies and constraints on potential formation mechanisms II: the northern hemisphere. Icarus 188, 324–344. https://doi.org/10.1016/j.icarus.2006.12.010.

Herschel, W., 1784. On the remarkable appearances at the polar regions of the planet Mars, and its spheroidical figure; with a few hints relating to its real diameter and atmosphere. Philos. Trans. R. Soc. 74, 233–273. https://doi.org/10.1098/rstl.1784.0020.

InSight Mars SEIS Data Service, 2019a. SEIS raw data, insight mission. IPGP, JPL, CNES, ETHZ, ICL, MPS, ISAE-Supaero, LPG, MFSC, https://doi.org/10.18715/SEIS.INSIGHT.XB_2016.

InSight Mars SEIS Data Service, 2019b. InSight SEIS data bundle. PDS Geosciences (GEO) Node, https://doi.org/10.17189/1517570.

InSight Marsquake Service, 2020. Mars seismic catalogue, InSight mission; V4 2020-10-01 (version 4.0). ETHZ, IPGP, JPL, ICL, MPS, Univ. Bristol, https://doi.org/10.12686/a9.

InSight Marsquake Service, 2021. Mars seismic catalogue, InSight mission; V5 2021-01-04 (version 5.0). ETHZ, IPGP, JPL, ICL, MPS, Univ. Bristol, https://doi.org/10.12686/a10.

Ivanov, B.A., 2001. Mars/Moon cratering rate ratio estimates. Space Sci. Rev. 96, 87–104. https://doi.org/10.1023/A:1011941121102.

JeongAhn, Y., Malhotra, R., 2015. The current impact flux on Mars and its seasonal variation. Icarus 262, 1–32. https://doi.org/10.1016/j.icarus.2015.08.032.

Kawamura, T., Lognonné, P., Nishikawa, Y., Tanaka, S., 2017. Evaluation of deep moonquake source parameters: implication for fault characteristics and thermal state. J. Geophys. Res. 122, 1487–1504. https://doi.org/10.1002/2016JE005147.

Knapmeyer, M., Oberst, J., Hauber, E., Wählisch, M., Deuchler, C., Wagner, R., 2006. Working models for spatial distribution and level of Mars' seismicity. J. Geophys. Res., Planets 111, E11006. https://doi.org/10.1029/2006JE002708.

Kullback, S., Leibler, R.A., 1951. On information and sufficiency. Ann. Math. Stat. 200, 79–86.

Lamp, J.L., Marchant, D.R., Mackay, S.L., Head, J.W., 2017. Thermal stress weathering and the spalling of Antarctic rocks. J. Geophys. Res., Earth Surf. 122, 3–24. https://doi.org/10.1002/2016JF003992.

Lockner, D.A., Beeler, N.M., 1999. Premonitory slip and tidal triggering of earthquakes. J. Geophys. Res. 104 (B9), 20133–201511. https://doi.org/10.1029/1999JB900205.

Lognonné, P., Banerdt, W.B., Giardini, D., Pike, W.T., Christensen, U., Laudet, P., de Raucourt, S., Zweifel, P., Calcutt, S., Bierwirth, M., Hurst, K.J., Ijpelaan, F., Umland, J.W., Llorca-Cejudo, R., Larson, S.A., Garcia, R.F., Kedar, S., Knapmeyer-Endrun, B., Mimoun, D., Mocquet, A., Panning, M.P., Weber, R.C., Sylvestre-Baron, A., Pont, G., Verdier, N., Kerjean, L., Facto, L.J., Gharakanian, V., Feldman, J.E., Hoffman, T.L., Klein, D.B., Klein, K., Onufer, N.P., Paredes-Garcia, J., Petkov, M.P., Willis, J.R., Smrekar, S.E., Drilleau, M., Gabsi, T., Nebut, T., Robert, O., Tillier, S., Moreau, C., Parise, M., Aveni, G., Ben Charef, S., Bennour, Y., Camus, T., Dandonneau, P.A., Desfoux, C., Lecomte, B., Pot, O., Revuz, P., Mance, D., tenPierick, J., Bowles, N.E.,

Charalambous, C., Delahunty, A.K., Hurley, J., Irshad, R., Liu, Huafeng, Mukherjee, A.G., Standley, I.M., Stott, A.E., Temple, J., Warren, T., Eberhardt, M., Kramer, A., Kühne, W., Miettinen, E.-P., Monecke, M., Aicardi, C., André, M., Baroukh, J., Borrien, A., Bouisset, A., Boutte, P., Brethomé, K., Brysbaert, C., Carlier, T., Deleuze, M., Desmarres, J.M., Dilhan, D., Doucet, C., Faye, D., Faye-Refalo, N., Gonzalez, R., Imbert, C., Larigauderie, C., Locatelli, E., Luno, L., Meyer, J.-R., Mialhe, F., Mouret, J.M., Nonon, M., Pahn, Y., Paillet, A., Pasquier, P., Perez, G., Perez, R., Perrin, L., Pouilloux, B., Rosak, A., Savin de Larclause, I., Sicre, J., Sodki, M., Toulemont, N., Vella, B., Yana, C., Alibay, F., Avalos, O.M., Balzer, M.A., Bhandari, P., Blanco, E., Bone, B.D., Bousman, J.C., Bruneau, P., Calef, F.J., Calvet, R.J., D'Agostino, S.A., de los Santos, G., Deen, R.G., Denise, R.W., Ervin, J., Ferraro, N.W., Gengl, H.E., Grinblat, F., Hernandez, D., Hetzel, M., Johnson, M.E., Khachikyan, L., Lin, J.Y., Madzunkov, S.M., Marshall, S.L., Mikellides, I.G., Miller, E.A., Raff, W., Singer, J.E., Sunday, C.M., Villalvazo, J.F., Wallace, M.C., Banfield, D., Rodriguez-Manfredi, J.A., Russell, C.T., Trebi-Ollennu, A., Maki, J.N., Beucler, E., Böse, M., Bonjour, C., Berenguer, J.L., Ceylan, S., Clinton, J., Conejero, V., Daubar, I., Dehant, V., Delage, P., Euchner, F., Estève, I., Fayon, L., Ferraioli, L., Johnson, C.L., Gagnepain-Beyneix, J., Golombek, M., Khan, A., Kawamura, T., Kenda, B., Labrot, P., Murdoch, N., Pardo, C., Perrin, C., Pou, L., Sauron, A., Savoie, D., Stähler, S., Stutzmann, E., Teanby, N.A., Tromp, J., van Driel, M., Wieczorek, M., Widmer-Schnidrig, R., Wookey, J., 2019. SEIS: insight's seismic experiment for internal structure of Mars. Space Sci. Rev. 215 (12). https://doi.org/10.1007/s11214-018-0574-6.

Lognonné, P., Banerdt, W.B., Pike, W.T., Giardini, D., Christensen, U., Garcia, R.F., Kawamura, T., Kedar, S., Knapmeyer-Endrun, B., Margerin, L., Nimmo, F., Panning, M., Tauzin, B., Scholz, J.-R., Antonangeli, D., Barkaoui, S., Beucler, E., Bissig, F., Brinkman, N., Calvet, M., Ceylan, S., Charalambous, C., Davis, P., van Driel, M., Drilleau, M., Fayon, L., Joshi, R., Kenda, B., Khan, A., Knapmeyer, M., Lekic, V., McClean, J., Mimoun, D., Murdoch, N., Pan, L., Perrin, C., Pinot, B., Pou, L., Menina, S., Rodriguez, S., Schmelzbach, C., Schmerr, N., Sollberger, D., Spiga, A., Stähler, S., Stott, A., Stutzmann, E., Tharimena, S., Widmer-Schnidrig, R., Andersson, F., Ansan, V., Beghein, C., Böse, M., Bozdag, E., Clinton, J., Daubar, I., Delage, P., Fuji, N., Golombek, M., Grott, M., Horleston, A., Hurst, K., Irving, J., Jacob, A., Knollenberg, J., Krasner, S., Krause, C., Lorenz, R., Michaut, C., Myhill, B., Nissen-Meyer, T., ten Pierick, J., Plesa, A.C., Quantin-Nataf, C., Robertsson, J., Rochas, L., Schimmel, M., Smrekar, S., Spohn, T., Teanby, N., Tromp, J., Vallade, J., Verdier, N., Vrettos, C., Weber, R., Banfield, D., Barrett, E., Bierwirth, M., Calcutt, S., Compaire, N., Johnson, C., Mance, D., Euchner, F., Kerjean, L., Mainsant, G., Mocquet, A., Antonio Rodriguez Manfredi, J., Pont, G., Laudet, P., Nebut, P., de Raucourt, S., Robert, O., Russel, C., Sylvestre-Baron, A., Tillier, S., Warren, T., Wieczorek, M., Yana, C., Zweifel, P., 2020. SEIS on Mars: first steps in comparative seismology between Mars, Earth and the Moon. Nat. Geosci. 13, 213–220. https://doi.org/10.1038/s41561-020-0536-y.

Lucas, A., Kenda, B., Mangeney, A., Kawamura, T., Daubar, I., Aharonson, O., Drilleau, M., Jacob, A., Hibert, C., Spiga, A., Rodriguez, S., Weber, R., Lognonné, P., 2019. Seismic detection of mass wasting on Mars with SEIS/InSight: a loony attempt? In: 50th Lunar and Planetary Science Conference. The Woodlands, TX, 18-22 March 2019. Abstract#2132.

Malin, M.C., Edgett, K.S., Posiolova, L.V., McColley, S.M., Noe Dobrea, E.Z., 2006. Present-day impact cratering rate and contemporary gully activity on Mars. Science 314, 1573–1577. https://doi.org/10.1126/science.1135156.

Manga, M., Zhai, G., Wang, C.-Y., 2019. Squeezing marsquakes out of groundwater. Geophys. Res. Lett. 46, 6333–6340. https://doi.org/10.1029/2019GL082892.

Martínez, G.M., Newman, C.N., De Vicente-Retortillo, A., Fischer, E., Renno, N.O., Richardson, M.I., Fairén, A.G., Genzer, M., Guzewich, S.D., Haberle, R.M., Harri, A.-M., Kemppinen, O., Lemmon, M.T., Smith, M.D., de la Torre-Juárez, M., Vasavada, A.R., 2017. The modern near-surface Martian climate: a review of in-situ meteoroligical data from Viking to Curiosity. Space Sci. Rev. 212, 295–338. https://doi.org/10.1007/s11214-017-0360-x.

Métivier, L., de Viron, O., Conrad, C.P., Renault, S., Diament, M., Patau, G., 2009. Evidence of earthquake triggering by the solid Earth tides. Earth Planet. Sci. Lett. 278, 370–375. https://doi.org/10.1016/j.epsl.2008.12.024.

Nakamura, Y., 2003. New identification of deep moonquakes in the apollo lunar seismic data. Phys. Earth Planet. Inter. 139, 197–205. https://doi.org/10.1016/j.pepi.2003.07.017.

Oberst, J., Nakamura, Y., 1987. Distinct meteoroid families identified on the lunar seismograms. J. Geophys. Res., Solid Earth 92 (B4), E769–E773. https://doi.org/10.1029/JB092iB04p0E769.

Ogata, Y., 1983. Estimation of the parameters in the modified Omori formula for aftershock frequencies by the Maximum Likelihood procedure. J. Phys. Earth 31, 115–124.

Phillips, R.J., 1991. Expected rates of marsquakes. In: Scientific Rationale and Requirements for a Global Seismic Network on Mars, LPI Tech. Rep. 91–02 LPI/TR-91–02. Lunar and Planet. Inst., Houston, Tex, pp. 35–38.

Plesa, A.-C., Knapmeyer, M., Golombek, M.P., Breuer, D., Grott, M., Kawamura, T., Lognonné, P., Weber, R.C., 2018. Present-day Mars' seismicity predicted from 3-D thermal evolution models of interior dynamics. Geophys. Res. Lett. 45. https://doi.org/10.1002/2017GL076124.

Roeloffs, E.A., 1988. Fault stability changes induced beneath a reservoir with cyclic variations in water level. J. Geophys. Res. 93 (B3), 2107–2124.

Rydelek, P.A., Davis, P.M., Koyanagi, R.Y., 1988. Tidal triggering of earthquake swarms at Kilauea Volcano, Hawaii. J. Geophys. Res. 93 (B5), 4401–4411. https://doi.org/10.1029/JB093iB05p04401.

Saxena, S.K., Metin Ger, A., Sengupta, A., 1988. Reservoir induced seismicity - a new model. Int. J. Numer. Anal. Methods Geomech. 12, 263–281.

Siegler, M.A., Smrekar, S.E., Grott, M., Piqueux, S., Mueller, N., Williams, J.-P., Plesa, A.-C., Spohn, T., 2017. The InSight Mars lander and its effect on the subsurface thermal environment. Space Sci. Rev. 211. https://doi.org/10.1007/s11214-017-0331-2.

Taylor, J., Teanby, N.A., Wookey, J., 2013. Estimates of seismic activity in the Cerberus Fossae region of Mars. J. Geophys. Res., Planets 118, 2570–2581. https://doi.org/10.1002/2013JE004469.

van Driel, M., Ceylan, S., Clinton, J.F., Giardini, D., Horleston, A., Margerin, L., Stähler, S.C., Böse, M., Charalambous, C., Kawamura, T., Khan, A., Orhand-Mainsant, G., Scholz, J.-R., Euchner, F., Knapmeyer, M., Schmerr, N., Pike, W.T., Lognonné, P., Banerdt, W.B., 2021. High frequency seismic events on Mars observed by InSight. J. Geophys. Res., Planets 126 (2). https://doi.org/10.1029/2020JE006670.